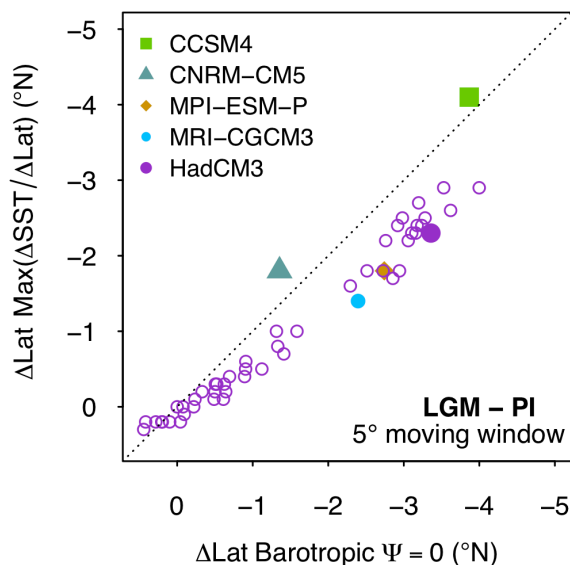


1 **Wind-driven evolution of the North Pacific subpolar gyre** 2 **over the last deglaciation**

3 *supporting information*

4 *Using planktic foraminiferal $\delta^{18}\text{O}_{\text{calcite}}$ to trace the gyre boundary*

5 Our ability to use the planktic foraminiferal $\delta^{18}\text{O}_{\text{calcite}}$ to trace the gyre boundary
6 comes from the dominance of the temperature signal over that of $\delta^{18}\text{O}_{\text{water}}$ in driving
7 the meridional pattern of $\delta^{18}\text{O}_{\text{calcite}}$ across the basin; the temperature signal is ~5 times
8 greater than the $\delta^{18}\text{O}_{\text{water}}$ (~salinity) signal (Figure 1). As the spatial temperature pattern
9 across the basin is primarily governed by the gyre circulation, with the steepest
10 meridional temperature gradient (and thus meridional $\delta^{18}\text{O}_{\text{calcite}}$ gradient) at the gyre
11 boundary, we can use the meridional profiles of temperature (~ $\delta^{18}\text{O}_{\text{calcite}}$) to track the
12 movement of the gyre boundary. Coupled climate models demonstrate a very tight
13 coupling between the LGM-PI change in latitude of gyre boundary (defined where
14 barotropic stream function = 0) and LGM-PI change in the latitude of maximum
15 latitudinal gradient in sea surface temperature (SST) (Figure S1). As no mechanism
16 exists to drive changes in $\delta^{18}\text{O}_{\text{water}}$ of the same magnitude as the changes in $\delta^{18}\text{O}_{\text{calcite}}$ -
17 _{water} fractionation from the large temperature difference between the gyres (Figure 1d),
18 the temperature signal will always dominate over the $\delta^{18}\text{O}_{\text{water}}$ signal in determining the
19 spatial pattern of $\delta^{18}\text{O}_{\text{calcite}}$ (Figure 1e) across the basin and the maximum meridional
20 $\delta^{18}\text{O}_{\text{calcite}}$ gradient (Figure 1f); thus, while there are likely to be local changes in $\delta^{18}\text{O}_{\text{water}}$
21 across the basin, the steepest part of the meridional $\delta^{18}\text{O}_{\text{calcite}}$ gradient will always be
22 determined by temperature, allowing us to use meridional profiles of $\delta^{18}\text{O}_{\text{calcite}}$ to track
23 the position of the gyre boundary through time.



24

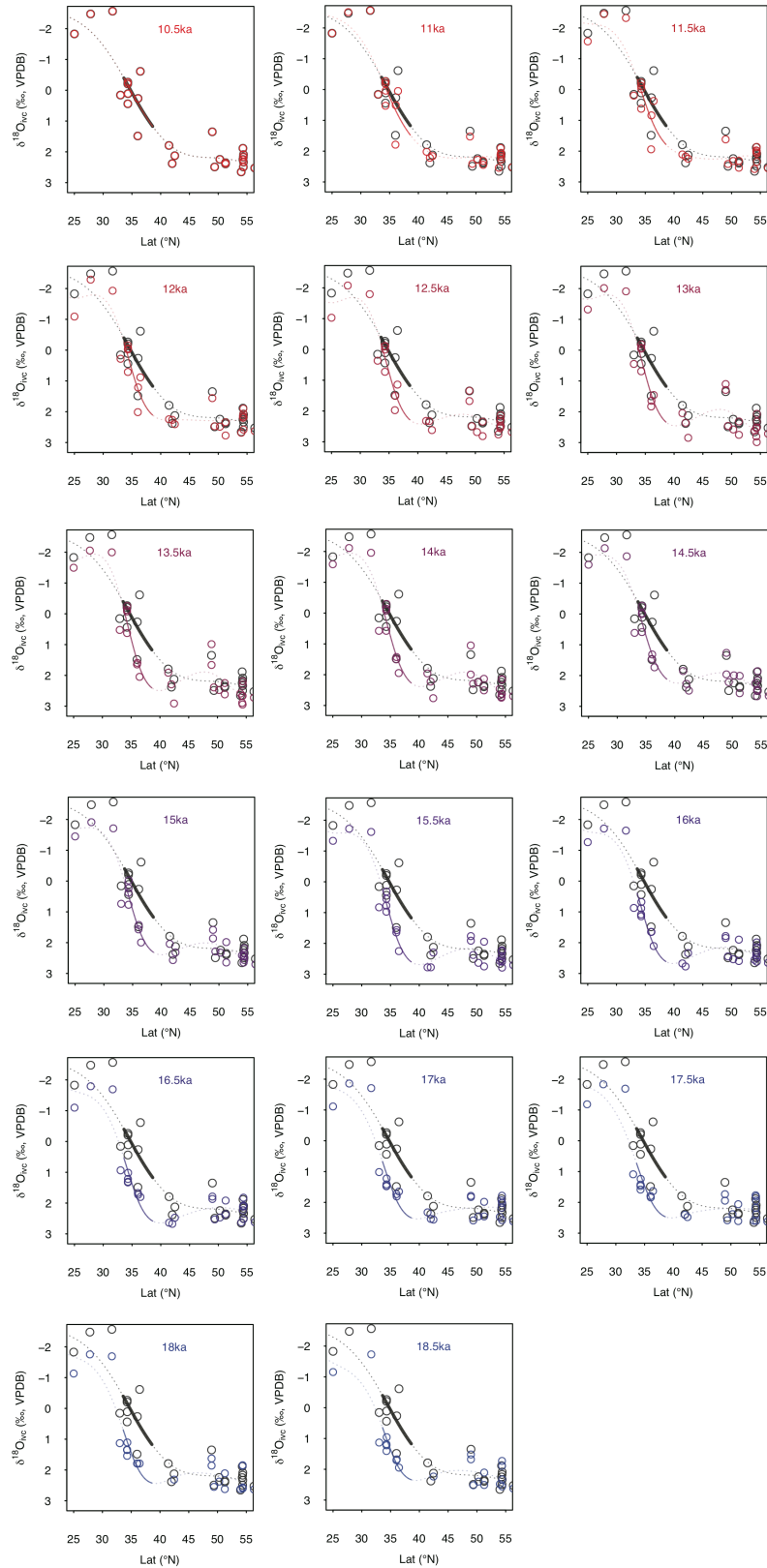
25 **Figure S1** Modelled zonal mean LGM-pre-industrial (PI) change in latitude of gyre boundary (defined
 26 where barotropic stream function = 0) versus LGM-PI change in latitude of maximum meridional
 27 gradient in sea surface temperature (SST) within a 5° moving window; the close relationship
 28 demonstrates past changes in the position of the maximum gradient in SST/Lat (and thus $\sim\delta^{18}\text{O}_{\text{calcite}}/\text{Lat}$)
 29 can be used to trace changes in the position of the gyre boundary.
 30

31 We model the $\delta^{18}\text{O}_{\text{calcite}}$ data as a function of latitude, using a general additive
 32 model (GAM) (Wood, 2011; Wood *et al.*, 2016) in the *mgcv* package in R (R core
 33 Team) at 500 yr timesteps from 18.5 to 10.5 ka (the time interval for which we have
 34 sufficient spatial and temporal resolution in our dataset; Figure 1),

35
$$\delta^{18}\text{O}_{\text{calcite}} = \beta + f(\text{Lat}) + \varepsilon$$

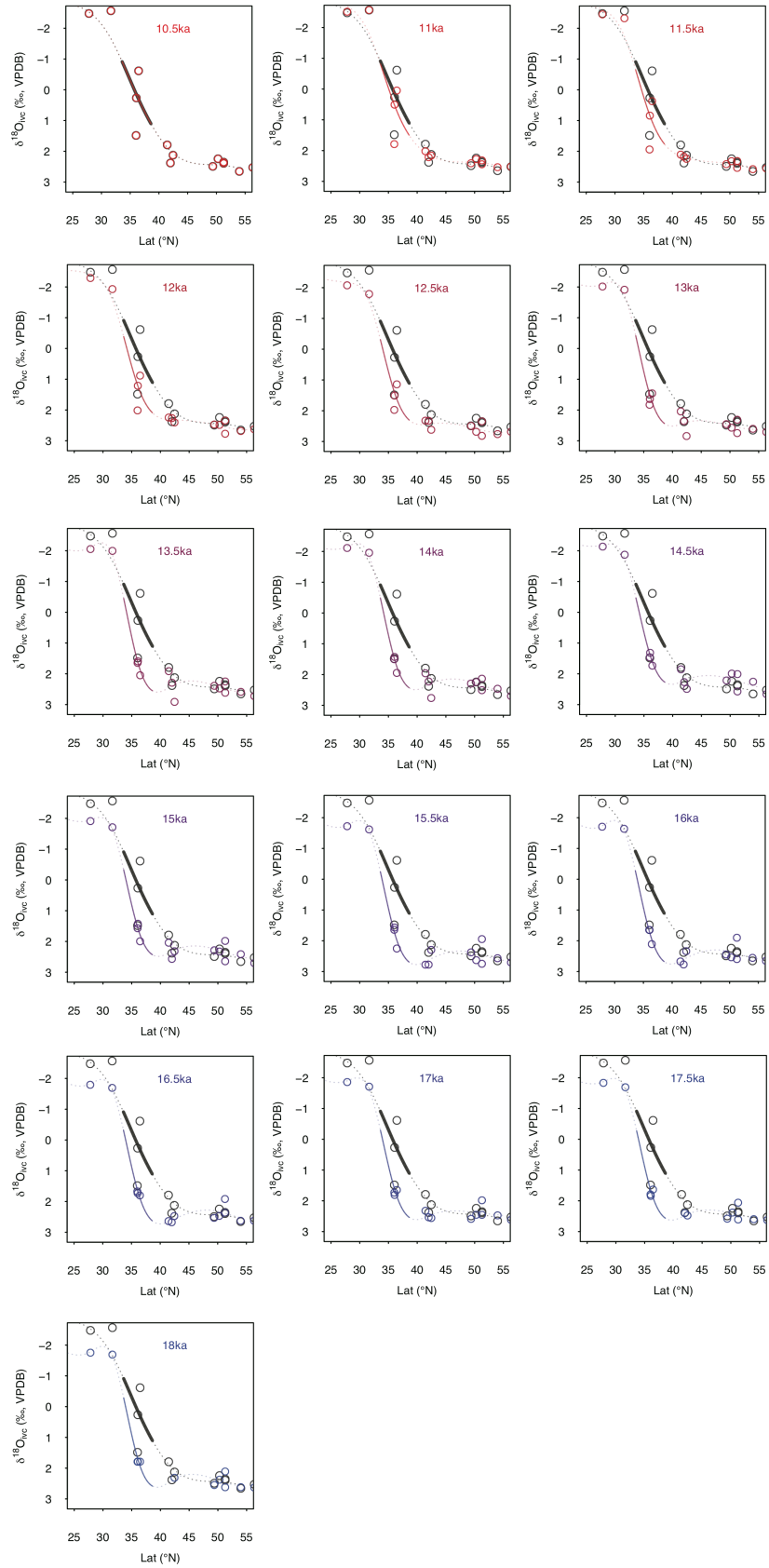
36 where $f(\text{Lat})$ is the sum of the underlying basis functions (Wood, 2011; Wood *et al.*,
 37 2016). The smoothing term (λ) was determined using generalised cross validation
 38 (GCV). We tested the models fitted using GCV by fitting models with an identical form,
 39 however using Reduced Maximum Likelihood (REML), which can sometimes be a
 40 preferable method to GCV (Reis and Ogden, 2009; Wood *et al.*, 2016), to determine
 41 the smoothing term; both GCV and REML result in identical smoothing terms, very
 42 similar degrees of freedom (4.06 with GCV versus 4.19 with REML), and
 43 indistinguishable model fits.

44



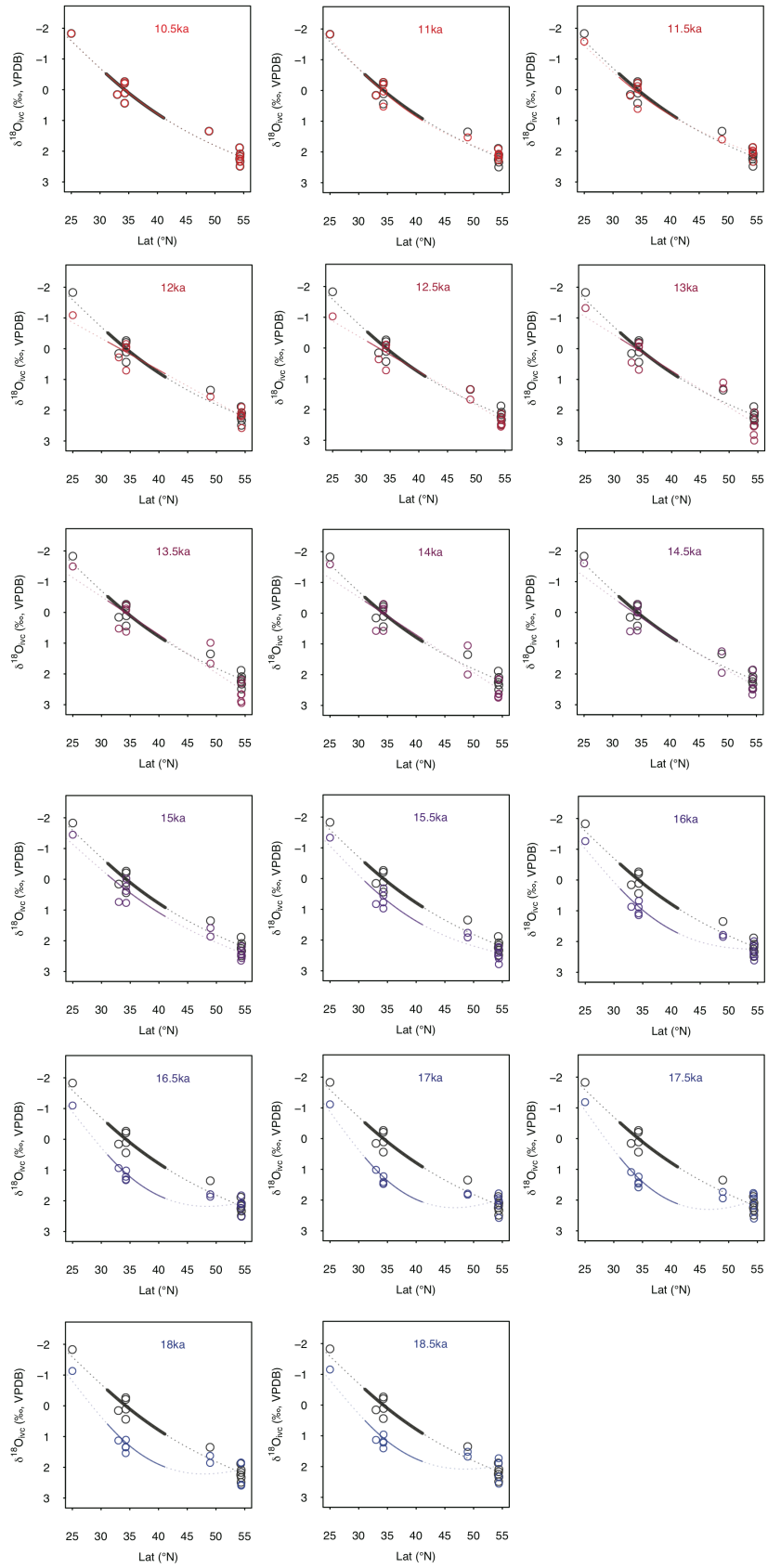
45

46 **Figure S2** GAM fits to $\delta^{18}\text{O}_{\text{calcite}}$ data as a function of latitude at 500 year timesteps from 18.5 to 10.5 ka
 47 (colours); the GAM fit to Holocene $\delta^{18}\text{O}_{\text{calcite}}$ data (10.5 ka) is shown in grey. The portion of the curve
 48 within the latitudinal band used to calculate the shift in gyre position is shown by the solid line; at each
 49 timestep we calculate the latitudinal shift that minimises the Euclidian distance between the solid part of
 50 the coloured curve and the solid part of the grey curve. Data are the combined east-west dataset (marked
 51 ALL on Figure 4).



52
53

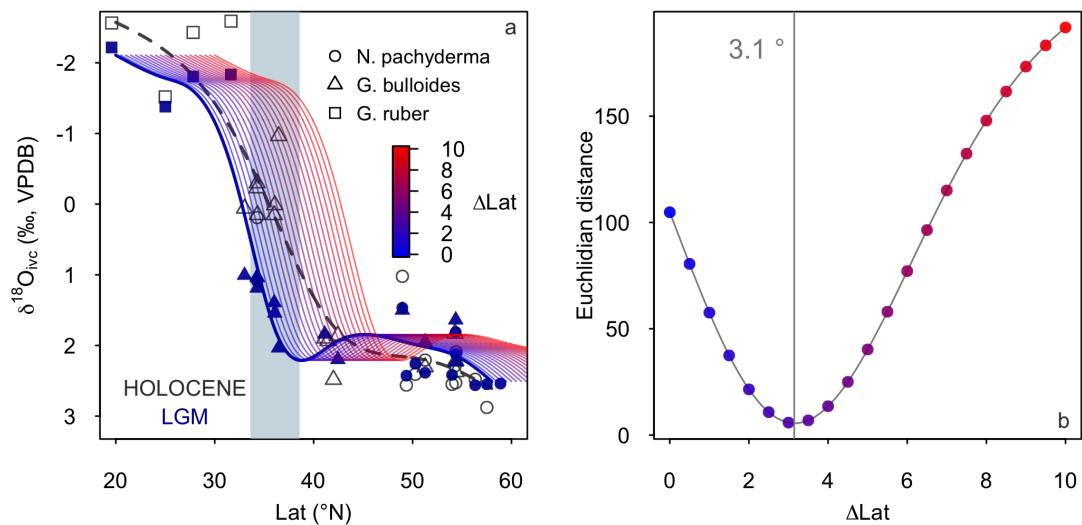
Figure S3 As figure SX, however data are from west of 180°.



54
55
56

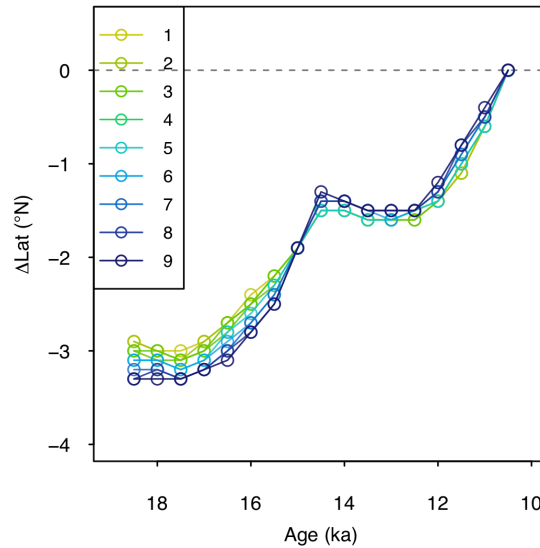
Figure S4 As figure SX, however data are from east of 180° .

57 We calculate the change in gyre boundary position over deglaciation as the
 58 latitudinal shift (x°) that minimises the Euclidian distance (L^2) between the Holocene
 59 (taken as 10.5 ± 0.5 ka) $\delta^{18}\text{O}_{\text{calcite}} \sim \text{latitude}$ GAM fit and the GAM fit to each time step,
 60 within a latitudinal band spanning the gyre boundary; this latitudinal band is centred
 61 around the maximum gradient in $\delta^{18}\text{O}_{\text{calcite}}$ versus latitude in the Holocene data within
 62 a 5° moving window (36.1°N). In the combined dataset from the east and west, and
 63 the data from the west only, we calculate the latitudinal shift using a 5° latitudinal band
 64 (i.e. 33.6 to 38.6°N), and we note the size of this latitudinal band has only a negligible
 65 effect on our results (Fig. SX); as the gyre boundary (and thus meridional temperature
 66 and $\delta^{18}\text{O}_{\text{calcite}}$ gradient) is more diffuse in the east, we use a slightly larger window of
 67 10° (i.e. 31.1 to 41.1°N).



68

69 **Figure S5** method used to calculate the shift in gyre boundary position **(a)** at each time step (here LGM,
 70 18.5 ka) we calculate the gyre boundary shift as the latitudinal shift (x° , in 0.1° increments from 0 to 10
 71 degrees) that minimises the Euclidian distance **(b)** within a specified latitudinal band (grey box in (a))
 72 between the GAM fit to the timestep and the Holocene in data is calculated. The coloured lines in (a)
 73 show the LGM GAM fit shifted north in 0.5° increments, and the coloured dots in (b) show the Euclidian
 74 distance at each increment, with the colour indicating the degree to which the curve has been shifted.
 75



76

77 **Figure S6 (a)** calculated change in the position of the gyre boundary using different sizes of latitudinal
 78 band (between 1° and 9°) in which the Euclidian distance is calculated; the size of latitudinal band (the
 79 grey box in figure SXa above) has very little effect on the results.
 80

81 We note that the steepest part of the Holocene curve ($\sim 36.1^\circ\text{N}$) using the
 82 combined dataset from the east and west, is further south than the zonal mean position
 83 of the gyre boundary today ($\sim 40^\circ\text{N}$). This is due to the westward bias within the dataset
 84 (i.e. there are many more sites in the west relative to the east within the dataset), and
 85 the gyre boundary is located slightly further south in the west relative to the zonal mean;
 86 the maximum meridional gradient in mean annual SST is found at $\sim 36^\circ\text{N}$ along the
 87 western margin of the basin (Boyer et al., 2013), in good agreement with our
 88 reconstruction.

89

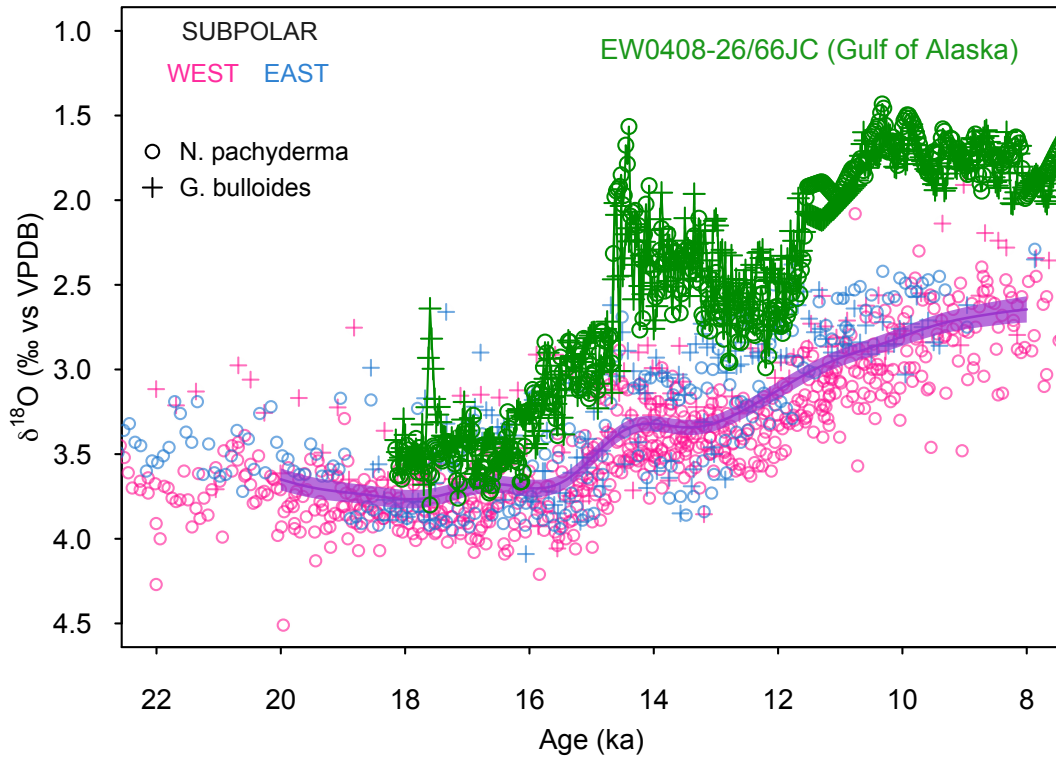
90 We also note that if we use a totally different method to calculate the change in
 91 position of the gyre boundary, simply calculating the change in latitude in the steepest
 92 part of the meridional $\delta^{18}\text{O}_{\text{calcite}}$ gradient (within a 5° moving window), we arrive at a
 93 very similar estimate of a $\sim 2.6^\circ$ southward shift between the Holocene and LGM. This
 94 method is more prone to anomalous values at the latitudinal extremes, hence we opt for
 95 the method of calculating the latitudinal shift that minimises the Euclidian distance

96 between timesteps within a defined latitudinal band described above; however, the
97 agreement between the two methods is reassuring.

98

99 *Planktic foraminiferal $\delta^{18}O_{\text{calcite}}$ compilation*

100 We compiled all available planktic foraminiferal calcite $\delta^{18}O$ from cores across the
101 North Pacific. All data were kept on the original age models, except in the case when
102 data were only available on uncalibrated ^{14}C age models, in which case the ^{14}C data
103 were recalibrated using INTCAL13 (Reimer et al., 2013) using an average of the
104 modern reservoir age at each site and a regional glacial increase of +400 years with
105 large uncertainties (± 500 years). All $\delta^{18}O_{\text{calcite}}$ data along with the core, location, water
106 depth, species, sediment depth, age, and original data reference are given in Table S1.
107 We only include cores spanning the interval between 10.5 to 18.5 ka with an average
108 resolution of >1 point per ka. We exclude core EW0408-26/66JC from the compilation
109 (Praetorius and Mix, 2014); this core is located in close proximity to the terminus of
110 a glacier and comparing the $\delta^{18}O_{\text{calcite}}$ data of this core to other cores within the subpolar
111 gyre demonstrates planktic foraminiferal $\delta^{18}O_{\text{calcite}}$ data from this core primarily reflect
112 local meltwater changes, rather than wider oceanographic conditions in the subpolar
113 gyre (Figure S3). The compiled dataset will be available on Pangea.



114

115 **Figure S7** Foraminiferal $\delta^{18}\text{O}_{\text{calcite}}$ from the subpolar gyre over deglaciation. A GAM fit with to all the
 116 data (excluding core EW0408-26/66JC) is shown by the purple line, with standard error of the fit shaded.
 117 Data from core EW0408-26/66JC (Praetorius and Mix, 2014) is shown in green.

118

119 *Seasonality of planktic foraminifera*

120 Our approach assumes that any change in seasonal bias relating to the habitat preference
 121 of foraminifera are small relative to the change in temperature due to the movement of
 122 the gyre boundary. The validity of this approach is supported by sites where $\delta^{18}\text{O}_{\text{calcite}}$
 123 has been measured on more than one species of foraminifera, such as core ODP Site
 124 893 (Figure 1 and Figure 2). At this site, foraminiferal species with habitat temperature
 125 preferences that are known to be different (*G. bulloides* and *N. pachyderma*, e.g. Taylor
 126 *et al.*, 2018) show very similar changes down core, with a Holocene-LGM change that
 127 is identical (within error); this suggests any changes relating to changes seasonal bias
 128 are likely to be insignificant in our reconstruction.

129

130

131 *Sea surface temperature compilation*

132 We compiled Mg/Ca and $U^{K'}_{37}$ sea surface temperature (SST) data from across the
133 North Pacific (Mg/Ca: Reitdorf et al., 2013; Gebhardt et al., 2008; Rodriguez Sanz et
134 al., 2013; Taylor et al., 2015; Sagawa et al., 2006; Sagawa et al., 2008; Pak et al., 2012;
135 Kubota et al., 2010; Gray et al., 2018. $U^{K'}_{37}$: Minoshima et al., 2007; Seki, 2004; Harada
136 et al., 2004; Harada, 2006; Harada et al., 2008; Inagaki et al., 2009; Herbert et al., 2001;
137 Sawada et al., 1998; Yamamoto et al., 2004; Isono et al., 2009). All age models are as
138 given in the original publication. All Mg/Ca and $U^{K'}_{37}$ data were recalibrated (see
139 below) and the temperature change during the LGM is given as a difference to both
140 proxy temperature in the Holocene, and to mean annual climatological temperature
141 from the WOA13 (Boyer et al., 2013).

142 While the direct temperature sensitivity of Mg/Ca in planktic foraminifera is ~6% per
143 °C (Gray et al., 2018b; Gray and Evans, 2019), due to the effect of temperature on pH
144 through the dissociation constant of water (K_w), the ‘apparent’ Mg/Ca temperature
145 sensitivity is higher (Gray et al., 2018b). Thus, we calculate the change in temperature
146 from the change in Mg/Ca at each site using a temperature sensitivity of 8.8%, derived
147 from laboratory cultures (Kisakürek et al., 2008), which encompasses both the direct
148 temperature effect and the temperature-pH effect, with a Mg/Ca-pH sensitivity of ~ -
149 8% per 0.1 pH unit (Lea et al., 1999; Russell et al., 2004; Evans et al., 2016; Gray et
150 al., 2018b; Gray and Evans, 2019). Mg/Ca is also influenced by salinity, with a
151 sensitivity of ~4% per PSU (Hönisch et al., 2013; Gray et al., 2018b; Gray and Evans,
152 2019). We make no attempt to account for the effects of salinity (due to sea level) or
153 pH downcore (due to lower atmospheric CO₂). The combined effect of the whole-ocean
154 increase in salinity (due to sea level), and the increase in surface ocean pH (due to lower
155 atmospheric CO₂) means changes in temperature derived from changes in Mg/Ca are

156 likely to be cold-biased by ~ 1.5 °C during the LGM (Gray and Evans, 2019). For UK^K₃₇,
157 the change in temperature at each site was calculated using the calibration of Prah1 et
158 al., 1988; the temperature range in this study is too low to be substantially effected by
159 the non-linearity of UK^K₃₇ (e.g. Tierney and Tingley, 2018).

160

161 *General Circulation Models*

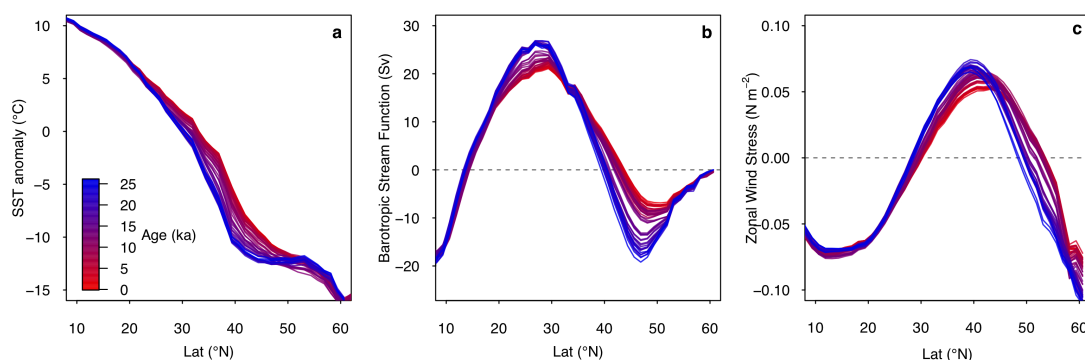
162 We assess differences in North Pacific barotropic stream function, wind stress curl,
163 zonal wind stress, and SST between LGM and pre-industrial conditions as represented
164 by five coupled climate models (CCSM4, CNRM-CM5, MPI-ESM-P and MRI-
165 CGCM3). All models are part of the Coupled Model Intercomparison Project phase 5
166 (CMIP5, Taylor et al., 2012). We only used models where both wind stress and
167 barotropic stream function data are available. Orbital parameters, atmospheric
168 greenhouse gas concentrations, coastlines and ice topography for the LGM simulations
169 are standardized as part of the Paleoclimate Model Intercomparison Project phase 3
170 (PMIP3) (Braconnot *et al.* 2012, Taylor *et al.* 2012). Ensemble means are computed by
171 first linearly interpolating to a common grid.

172

173 Using a single model (HadCM3) we look at runs where the model greenhouse gas, ice
174 sheet albedo, ice sheet topography are changed individually (‘Green Mountains, White
175 Plains’) as described in Roberts and Valdes (2017). The ‘Green Mountains, White
176 Plains’ runs use the ICE5G ice sheet reconstruction (Peltier *et al.*, 2004), whereas the
177 deglacial ‘snapshot’ runs (below) use the ICE6G ice sheet reconstruction (Peltier *et al.*,
178 2015).

179

180 We also explore changes through time over the deglaciation using a series of HadCM3
181 equilibrium-type simulations where all forcings and model boundary conditions are
182 changed at 500-year intervals broadly adhering to the PMIP4 last deglaciation protocol
183 (Ivanovic et al., 2016). These simulations use the ICE6GC ice sheet reconstruction and
184 'melt-uniform' scenario for ice sheet meltwater; i.e. freshwater from the melting ice
185 sheets is NOT routed to the ocean via coastal outlets. Instead, water is conserved by
186 forcing the global mean ocean salinity to be consistent with the change in global ice
187 sheet volume with respect to present. Note, these deglacial simulations are not transient,
188 but are equilibrium-type experiments that begin from the end of the 1750-year long
189 simulations run by Singarayer et al. (2011). At each 500-year interval (21.0 ka, 20.5 ka,
190 20.0 ka...0.5 ka, 0.0 ka), all boundary conditions and forcings are updated according to
191 the more recent literature (presented by Ivanovic et al., 2016) and held constant for the
192 full 500-year duration of the run. The climate means and standard deviations used here
193 are calculated from the last 50 years of each simulation (i.e. year 451-500, inclusive).
194 More information on these runs can be found in the supplement to Morris et al. (2018),
195 noting that we use the raw model output and not the downscaled and bias-corrected
196 data used in the previous publication.



197

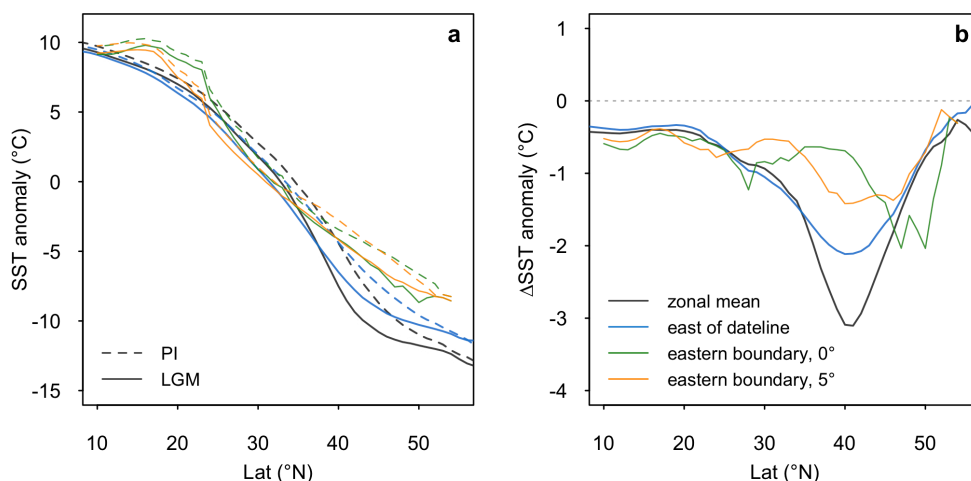
198 **Figure S8** Deglacial evolution of zonal mean (a) SST anomaly (relative to global mean) (b) barotropic
199 stream function (c) zonal wind stress in the HadCM3 simulations.

200

201

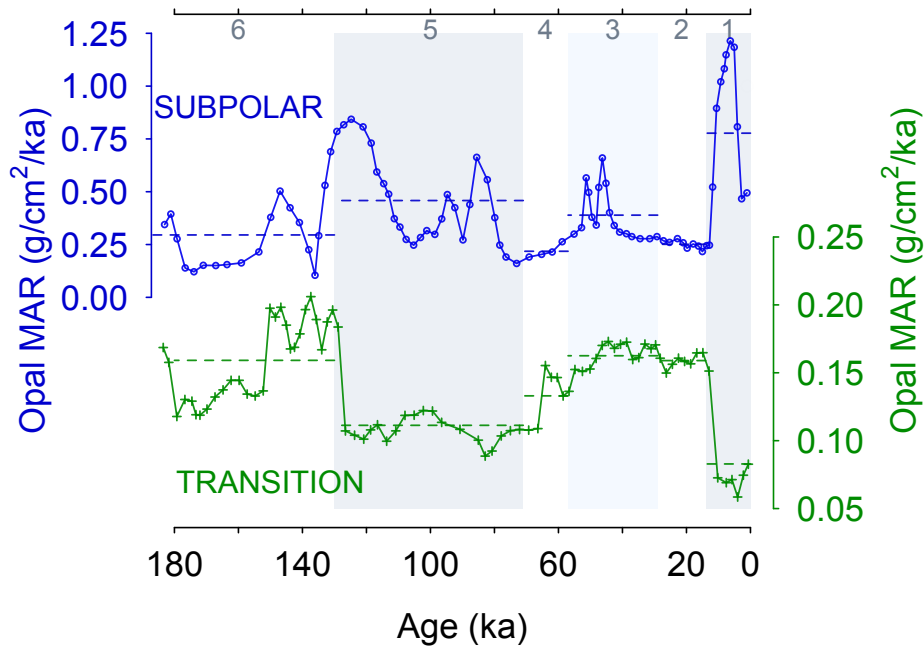
202 *Eastern boundary test*

203 To test if there is an influence of coastal upwelling on the data in the east (i.e. a signal
204 of some other control on latitudinal temperature anomaly [and thus latitudinal $\delta^{18}\text{O}_{\text{calcite}}$
205 anomaly] besides change in gyre position) we compare the ensemble mean SST along
206 the eastern boundary of the basin (taken as the first oceanic grid point west of land
207 during the LGM) to the zonal mean, and zonal mean east of the dateline (Fig. S9). The
208 models show no indication of a strong influence of coastal upwelling, which would
209 manifest as an anomalous cooling relative to the zonal mean. This analysis suggests
210 coastal upwelling is unlikely to be having a significant effect on our results, although
211 the simulated coastal upwelling may be poorly represented due to the resolution of the
212 models. A further argument against a strong influence of upwelling on the data in the
213 East Pacific is that sites that are $\sim 15^\circ$ apart from each other latitudinally, such that they
214 are in different upwelling regimes today and are likely to have undergone very different
215 changes in upwelling since the LGM, display very similar patterns of change in
216 $\delta^{18}\text{O}_{\text{calcite}}$ over deglaciation, with no differences in timing (Fig. 1).



217

218 **Figure S9 (a)** LGM and PI SST anomaly (from global mean), and **(b)** LGM-PI SST anomaly in different
219 longitudinal bins; zonal mean (grey), zonal mean east of the dateline (180°, blue), along the eastern
220 boundary of the basin (green), and 5° seaward from the eastern boundary of the basin (orange). Note, the
221 gyre boundary is located slightly further north along the eastern margin relative to the zonal mean and
222 zonal mean east of the dateline.
223



224

225 **Figure S10** Opal Mass Accumulation Rate data from core KH99-03 in the SPG (Narita et al., 2002) and
 226 core NCG108 in the transition zone (Maeda et al., 2002). Dashed lines show mean value for each marine
 227 isotope stage (MIS). Grey shading shows MIS 1, 3 and 5. Transition zone and subpolar waters show an
 228 anti-phased relationship in Opal MAR over the last glacial cycle.
 229

230 *HSI Freshwater test*

231 The release of large amounts of freshwater into the eastern subpolar North Pacific has
 232 been suggested over deglaciation, at ~17.5 ka (Maier *et al* 2018). The release of
 233 freshwater into the eastern subpolar North Pacific is evident in an increase in the
 234 $\delta^{18}\text{O}_{\text{calcite}}$ difference between the mixed-layer dwelling species *G. bulloides* and the
 235 slightly deeper-dwelling species *N. pachyderma* in core MD02-2489 (54.39°N, -
 236 148.92°E) at this time; during this interval *G. bulloides* becomes ~0.6‰ more depleted
 237 than *N. pachyderma*. To test if this release of freshwater may be influencing our gyre
 238 boundary reconstruction we re-run the gyre-boundary analysis, however removing the
 239 *G. bulloides* data from core MD02-2489; the results are identical to the gyre boundary
 240 reconstruction including the *G. bulloides* data demonstrating that the effect of
 241 freshwater release has very little effect on our gyre boundary reconstruction. This is
 242 because the change in $\delta^{18}\text{O}_{\text{calcite}}$ from the freshwater release (~0.6‰, equivalent to ~2

243 PSU freshening) is very small compared to the large change in $\delta^{18}\text{O}_{\text{calcite}}$ resulting from
244 the temperature difference between the gyres (6 ‰). Localised freshwater inputs, while
245 having a large effect locally, do very little to change the pattern of $\delta^{18}\text{O}_{\text{calcite}}$ at the basin
246 scale.

247

248

249

250

251

252

253

254

255

256

257

258

259

260

261

262

263

264

265

266

267

268

269

270

271

Table S1 Compiled planktic foraminiferal $\delta^{18}\text{O}_{\text{calcite}}$ records. The compiled will be made available on Pangea.

Core	Lat (°N)	Lon (°E)	Species	Reference
MD02-2489	54.39	-148.921	N. pachyderma	Gebhardt et al 2008
MD02-2489	54.39	-148.921	G. bulloides	Gebhardt et al 2008
PAR87A-10	54.363	-148.4667	G. bulloides	Zahn et al 1991
PAR87A-10	54.363	-148.4667	N. pachyderma	Zahn et al 1991
PAR87A-02	54.29	-149.605	G. bulloides	Zahn et al 1991
PAR87A-02	54.29	-149.605	N. pachyderma	Zahn et al 1991
MD02-2496	48.967	-127.033	N. pachyderma	Taylor et al 2015
MD02-2496	48.967	-127.033	G. bulloides	Taylor et al 2015
ODP1017	34.32	-121.6	G. bulloides	Pak et al 2012
ODP893	34.2875	-120.03667	N. pachyderma	Hendy et al 2002
ODP893	34.2875	-120.03667	G. bulloides	Hendy et al 2002
MD02-2503	34.28	-120.04	G. bulloides	Hill et al 2006
AHF-28181	33.011667	-119.06	G. bulloides	Mortyn et al 1996
MD05-2505	25	-112	G. ruber	Rodríguez-Sanz et al 2013
SO201-2-101	58.883	170.683	N. pachyderma	Reitdorf et al 2013
SO201-2-85	57.505	170.413167	N. pachyderma	Reitdorf et al 2013
SO201-2-77	56.33	170.69883	N. pachyderma	Reitdorf et al 2013
SO201-2-12	53.992667	162.375833	N. pachyderma	Reitdorf et al 2013
MD01-2416	51.268	167.725	N. pachyderma	Gebhardt et al 2008
MD01-2416	51.268	167.725	G. bulloides	Gebhardt et al 2008
VINO-GGC37	50.28	167.7	N. pachyderma	Keigwin 1998
LV29-114-3	49.375667	152.877933	N. pachyderma	Reitdorf et al 2013
KT90-9_21	42.45	144.3167	G. bulloides	Oba and Murayama 2004
GH02-1030	42	144	G. bulloides	Sagawa and Ikehara 2008
CH84-14	41.44	142.33	G. bulloides	Labeyrie 1996
CH84-04	36.46	142.13	G. bulloides	Labeyrie 1996
MD01-2420	36.067	141.817	G. bulloides	Sagawa et al 2006
MD01-2421	36.01667	141.7833	G. bulloides	Oba and Murayama 2004
KY07_04_01	31.6391667	128.944	G. ruber	Kubota et al 2010
A7	27.82	126.98	G. ruber	Sun et al 2005
ODP184-1145	19.58	117.63	G. ruber	Oppo and Sun 2005

272

273

274

275

276

277

278

Table S2 Reconstructed change in gyre boundary latitude. Uncertainty is 1σ .

age	DLat	DLat_error	DLat_west	DLat_west_error	Dlat_east	DLat_east_error
10.5	0.0	1.0	0.0	1.3	0	1.0
11.0	-0.6	0.9	-0.7	1.2	-0.3	0.9
11.5	-1.0	0.9	-1.1	1.1	-0.5	1.0
12.0	-1.4	0.9	-1.7	1.1	-0.5	1.1
12.5	-1.5	0.9	-1.9	1.0	-0.8	1.1
13.0	-1.6	0.9	-1.8	1.0	-0.2	1.3
13.5	-1.6	0.9	-1.8	1.0	0	1.3
14.0	-1.5	0.9	-1.7	1.0	0.2	1.3
14.5	-1.5	0.9	-1.7	1.0	-0.5	1.2
15.0	-1.9	0.8	-1.9	1.0	-2.4	1.0
15.5	-2.3	0.8	-2.1	1.0	-3.9	1.0
16.0	-2.6	0.8	-2.1	1.0	-5	0.9
16.5	-2.8	0.9	-2.0	1.0	-5.9	0.9
17.0	-3.1	0.9	-2.0	1.0	-6.3	0.9
17.5	-3.2	0.9	-2.0	1.0	-6.3	1.0
18.0	-3.1	0.9	-2.0	1.0	-6.4	1.1
18.5	-3.1	0.9	NA	NA	-6	1.1

279

280 **Additional References**

- 281 Boyer, T.P., Antonov, J.I., Baranova, O.K., Coleman, C., Garcia, H.E., Grodsky, A., John-
282 R.A., Mishonov, A.V., O'Brien, T.D., Paver, C.R., Reagan, J.R., Seidov, D., Smolyar, I.V., Zweng, M.M., 2013.
283 World Ocean Database 2013. In: Levitus, Sydney (Ed.), Alexey Mishonov (Technical Ed.), NOAA Atlas
284 NESDIS, vol. 72. 209 pp.
- 285 Evans D., Wade B. S., Henehan M., Erez J. and Müller W. (2016) Revisiting carbonate chemistry controls on
286 planktic foraminifera Mg / Ca: Implications for sea surface temperature and hydrology shifts over the Paleocene-
287 Eocene Thermal Maximum and Eocene-Oligocene transition. *Clim. Past* 12.
- 288 Gebhardt, H. et al., Paleonutrient and productivity records from the subarctic North Pacific for Pleistocene glacial
289 terminations I to V. *Paleoceanography* 23, PA4212 (2008).
- 290 Gray, W. R., Weldeab, S., Lea, D. W., Rosenthal, Y., Gruber, N., Donner, B. and Fischer, G. (2018b) The effects of
291 temperature, salinity, and the carbonate system on Mg/Ca in *Globigerinoides ruber* (white): A global sediment
292 trap calibration. *Earth Planet. Sci. Lett.* 482, 607–620.
- 293 Gray, W.R. and Evans, D. (2019) Nonthermal influences on Mg/Ca in planktonic foraminifera: A review of culture
294 studies and application to the last glacial maximum. *Paleoceanography and Paleoclimatology*, 34. [https://doi.org/](https://doi.org/10.1029/2018PA003517)
295 [10.1029/2018PA003517](https://doi.org/10.1029/2018PA003517)
- 296 Harada, N. Ahagon, N., Uchida, M. (2004) Northward and southward migrations of frontal zones during the past 40
297 kyr in the Kuroshio-Oyashio transition area. *Geochemistry*, doi:10.1029/2004GC000740/pdf.
- 298 Harada, N. (2006) Rapid fluctuation of alkenone temperature in the southwestern Okhotsk Sea during the past 120
299 ky. *Global and Planetary Change*. 53, 29–46.
- 300 Harada, N., Sato, M., Sakamoto, T. (2008) Freshwater impacts recorded in tetraunsaturated alkenones and alkenone
301 sea surface temperatures from the Okhotsk Sea across millennial-scale cycles. *Paleoceanography*. 23, PA3201.
- 302 Harada, N., Sato, M., Sakamoto, T. (2008) Freshwater impacts recorded in tetraunsaturated alkenones and alkenone
303 sea surface temperatures from the Okhotsk Sea across millennial-scale cycles. *Paleoceanography*. 23, PA3201.
- 304 Hendy, I. L., Kennett, J. P., Roark, E. B., Ingram, B. L., (2002) Apparent synchronicity of submillennial scale climate
305 events between Greenland and Santa Barbara Basin, California from 30-10 ka. *Quaternary Science Reviews* 21,
306 1167-1184.
- 307 Herbert, D. et al. (2001) Collapse of the California Current During Glacial Maxima Linked to Climate Change on
308 Land. *Science*. 293, 71–76.

309 Hill, T.M., J.P. Kennett, D.K. Pak, R.J. Behl, C. Robert, and L. Beaufort. 2006. Pre-Bolling warming in Santa
310 Barbara Basin, California: surface and intermediate water records of early deglacial warmth. *Quaternary Science*
311 *Reviews* 25, pp. 2835–2845, doi:10.1016/j.quascirev.2006.03.012

312 Hönlisch B., Allen K. a., Lea D. W., Spero H. J., Eggins S. M., Arbuszewski J., deMenocal P., Rosenthal Y., Russell
313 A. D. and Elderfield H. (2013) The influence of salinity on Mg/Ca in planktic foraminifers – Evidence from
314 cultures, core-top sediments and complementary $\delta^{18}\text{O}$. *Geochim. Cosmochim. Acta* 121, 196–213.

315 Inagaki, M., Yamamoto, M., Igarashi, Y., Ikehara, K. (2009) Biomarker records from core GH02-1030 off Tokachi
316 in the northwestern Pacific over the last 23,000 years: Environmental changes during the last deglaciation.
317 *Journal of Oceanography*. 65, 847–858.

318 Isono, D. et al. (2009) The 1500-year climate oscillation in the midlatitude North Pacific during the Holocene.
319 *Geology*. 37, 591–594.

320 Kisakürek, B., Eisenhauer, A., Böhm, F., Garbe-Schönberg, D., Erez, J., 2008. Controls on shell Mg/Ca and Sr/Ca
321 in cultured planktonic foraminiferan, *Globigerinoides ruber* (white). *Earth Planet. Sci. Lett.* 273, 260–269.
322 <https://doi.org/10.1016/j.epsl.2008.06.026>.

323 Kubota, Y., K. Kimoto, R. Tada, H. Oda, Y. Yokoyama, and H. Matsuzaki (2010), Variations of East Asian summer
324 monsoon since the last deglaciation based on Mg/Ca and oxygen isotope of planktic foraminifera in the northern
325 East China Sea, *Paleoceanography*, 25, PA4205, doi:10.1029/2009PA001891.

326 Labeurie, L. 1996. Quaternary paleoceanography: unpublished stable isotope records. IGBP PAGES/World Data
327 Center for Paleoclimatology Data Contribution Series #1996-036. NOAA/NGDC Paleoclimatology Program,
328 Boulder, Colorado, USA.

329 Lea D. W., Mashiotta T. A. and Spero H. J. (1999) Controls on magnesium and strontium uptake in planktonic
330 foraminifera determined by live culturing. *Geochim. Cosmochim. Acta* 63, 2369–2379.

331 Maeda, L., H. Kawahata and M. Noharta (2002): Fluctuation of biogenic and abiogenic sedimentation on the Shatsky
332 Rise in the western north Pacific during the late Quaternary. *Marine Geology* 189, 197-214.

333 Minoshima, K., H. Kawahata, K. Ikehara (2007) Changes in biological production in the mixed water region (MWR)
334 of the northwestern North Pacific during the last 27 kyr. *Palaeogeography, Palaeoclimatology, Palaeoecology*.
335 254, 430–447.

336 Mortyn, P. G., Thunell, R. C., Anderson, D. M., Stott, L. D., Le, J. (1996) Sea surface temperature changes in the
337 Southern California Borderlands during the last glacial-interglacial cycle. *Paleoceanography* 11, 415-430.

338 Narita, H., M. Sato, S. Tsunogai, M. Maruyama, M. Ikehara, T. Nkatsuka, M. Wakatsuchi, N. Harada and U. Ujiie
339 (2002): Biogenic opal indicating less productive northwestern North Pacific during glacial stages. *Geophys. Res.*
340 *Lett.*, 29(15), 22-1 to 22-4.

341 Oba, T., Murayama, M. (2004) Sea-surface temperature and salinity changes in the northwest Pacific since the Last
342 Glacial Maximum. *Journal of Quaternary Science* 19, 335-346.

343 Oppo, D. W., and Y. Sun (2005) Amplitude and timing of sea surface temperature change in the northern South
344 China Sea: Dynamic link to the East Asian monsoon. *Geology* 33, 785–788.

345 Pak, D. K., D. W. Lea, and J. P. Kennett (2012) Millennial scale changes in sea surface temperature and ocean
346 circulation in the northeast Pacific, 10–60 kyr BP, *Paleoceanography* 27, PA1212, doi:10.1029/2011PA002238.

347 Peltier, W. R. (2004). Global glacial isostasy and the surface of the Ice-Age Earth: The ICE-5G (VM2) model and
348 GRACE. *Annual Review of Earth and Planetary Sciences*, 32(1), 111–149.
349 <https://doi.org/10.1146/annurev.earth.32.082503.144359>

350 Praetorius, S. K., Mix, A. C. (2014) Synchronization of North Pacific and Greenland climates preceded abrupt
351 deglacial warming. *Science* 345, 444. DOI: 10.1126/science.1252000.

352 Prahl, F. G., L. A. Muehlhausen, and D. L. Zahnle (1988), Further evaluation of long-chain alkenones as indicators
353 of paleoceanographic conditions, *Geochim. Cosmochim. Acta* 52, 2303–2310.

354 Reimer, P. J. et al. (2013) IntCal13 and Marine13 radiocarbon age calibration curves 0-50,000 years cal BP.
355 *Radiocarbon* 55, 1869–1887.

356 Reiss, P. T., Ogden, R. T. (2009) Smoothing parameter selection for a class of semiparametric linear models. *Journal*
357 *of the Royal Statistical Society B* 71, 505-523.

358 Riethdorf, J.-R., Max, L., Nürnberg, D., Lembke-Jene, L., Tiedemann, R. (2013) Deglacial development of (sub)
359 sea surface temperature and salinity in the subarctic northwest Pacific: Implications for upper-ocean
360 stratification. *Paleoceanography*. 28, 91–104.

361 Rodríguez Sanz, L., Mortyn, P. G., Herguera, J. C., Zahn, R. (2013) Hydrographic changes in the tropical and
362 extratropical Pacific during the last deglaciation. *Paleoceanography*. 28, 529–538.

363 Russell A. D., Hönlisch B., Spero H. J. and Lea D. W. (2004) Effects of seawater carbonate ion concentration and
364 temperature on shell U, Mg, and Sr in cultured planktonic foraminifera. *Geochim. Cosmochim. Acta* 68, 4347–
365 4361.

- 366 Sagawa, T., Toyoda, K., Oba, T. (2006) Sea surface temperature record off central Japan since the Last Glacial
367 Maximum using planktonic foraminiferal Mg/Ca thermometry.
- 368 Sagawa, T., Ikehara, K. (2008) Intermediate water ventilation change in the subarctic northwest Pacific during the
369 last deglaciation. *Geophysical Research Letters* 35, L24702, doi:10.1029/2008GL035133.
- 370 Seki, O., et al. (2004) Reconstruction of paleoproductivity in the Sea of Okhotsk over the last 30 kyr.
371 *Paleoceanography*. 19, PA1016.
- 372 Singarayer, J.S., Valdes, P.J., Friedlingstein, P., Nelson, S., Beerling, D.J., 2011. Late Holocene methane rise caused
373 by orbitally controlled increase in tropical sources. *Nature* 470, 8285. <https://doi.org/10.1038/nature09739>
- 374 Taylor, B.J., Rae, J.W.B., Gray, W.R., Darling, K.F., Burke, A., Gersonde, R., Abelman, A., Maier, E., Esper, O.,
375 Ziveri, P. (2018) Distribution and ecology of planktic foraminifera in the North Pacific: Implications for paleo-
376 reconstructions. *Quaternary Science Reviews* 191, 256-274.
- 377 Taylor, M. A., Hendy, I. L., Pak, D. K. (2014) Deglacial ocean warming and marine margin retreat of the Cordilleran
378 Ice Sheet in the North Pacific Ocean. *Earth and Planetary Science Letters*. 403, 89–98 (2014).
- 379 Tierney J. E. and Tingley M. P. (2018) BAYSPLINE: A New Calibration for the Alkenone Paleothermometer.
380 *Paleoceanogr. Paleoclimatology* 33, 281–301.
- 381 Yamamoto, M., Oba, T., Shimamune, J., Ueshima, T. (2004) Orbital-scale anti-phase variation of sea surface
382 temperature in mid-latitude North Pacific margins during the last 145,000 years. *Geophysical Research Letters*.
383 31, L16311.
- 384 Zahn, R., Pedersen, T. F., Bornhold, B. D., Mix, A. C. (1991) Watermass conversion in the glacial subarctic Pacific
385 (54°N, 148°W): physical constraints and the benthic-planktonic stable isotope record. *Paleoceanography* 6, 543-
386 560.